

OPEN ACCESS

EDITED BY

Alexander Marshak, Climate and Radiation Lab, Goddard Space Flight Center, National Aeronautiacs and Space Administration, United States

REVIEWED BY

T. John Tharakan, Indian Space Research Organisation, India Antti Arola, Chinese Academy of Sciences, Finland

*CORRESPONDENCE

Omar Torres,

⋈ omar.o.torres@nasa.gov

RECEIVED 13 August 2025
REVISED 03 October 2025
ACCEPTED 15 October 2025

ACCEPTED 15 October 2025
PUBLISHED 14 November 2025

CITATION

Torres O, Jethva H, Ahn C and Kayetha V (2025) A decade of global hourly aerosol observations from DSCOVR/EPIC using near-UV measurements.

Front. Remote Sens. 6:1685415. doi: 10.3389/frsen.2025.1685415

COPYRIGHT

© 2025 Torres, Jethva, Ahn and Kayetha. This is an open-access article distributed under the terms of the Creative Commons Attribution License (CC BY). The use, distribution or reproduction in other forums is permitted, provided the original author(s) and the copyright owner(s) are credited and that the original publication in this journal is cited, in accordance with accepted academic practice. No use, distribution or reproduction is permitted which does not comply with these terms.

A decade of global hourly aerosol observations from DSCOVR/EPIC using near-UV measurements

Omar Torres^{1*}, Hiren Jethva^{1,2}, Changwoo Ahn³ and Vinay Kayetha³

¹Atmospheric Chemistry and Dynamics Laboratory, NASA Goddard Space Flight Center, Greenbelt, MD, United States, ²Morgan State University, GESTAR-II, Baltimore, MD, United States, ³Science Systems and Applications, Inc., Lanham, MD, United States

The availability of air quality (AQ) and climate related satellite information from the Earth Polychromatic Imaging Camera (EPIC) on the Deep Space Climate Observatory (DSCOVR), at the Lagrange Point 1 (L1) orbital configuration significantly enhances the diurnal coverage over large areas of the Sunlit side of the globe. The simultaneous availability of L1 and Geostationary (GEO) observations, along with traditional low-Earth- orbit (LEO) satellite measurements, offers a unique opportunity for the integration of a truly global AQ-observing system. In this paper, we discuss the decadal aerosol record from near-UV observations made by the EPIC-DSCOVR sensor. The near-UV EPIC aerosol record (EPICAERUV) shows a large increase in the atmospheric carbonaceous aerosol load over the last decade. In addition to the wellknown seasonally varying sources of carbonaceous aerosols produced by biomass burning, a new source of carbonaceous particulate associated primarily, but not exclusively, with wildfires in the northern hemisphere has emerged and has been consistently detected over the last 10 years by EPIC and other spaceborne sensors. Unlike biomass burning aerosols produced in tropical and sub-tropical regions and, generally, residing in the lower troposphere, carbonaceous aerosols from wildfires in mid and high-latitude regions often ascend to the middle and high troposphere and, in some instances, reach the lower stratosphere where their residence time is significantly longer than in the troposphere. Wildfires and severe dust storms over the last decade have been observed by EPIC on a global basis from Australia and Chile in the Southern Hemisphere to North America, Central Europe, Siberia, and China in the Northern Hemisphere. We show and document some of these prominent aerosol events using the EPICAERUV aerosol dataset.

KEYWORDS

DSCOVR, EPIC, Lagrange 1 point, near-UV absorption, carbonaceous smoke, decadal record, mineral dust

1 Introduction

The spatial extent and temporal evolution of carbonaceous aerosol layers associated with biomass burning and wildfires are monitored by means of satellite observations. Over the last decade, spaceborne atmospheric composition remote sensing has benefited from the availability of UV-to-near IR multi-spectral observations from satellite-borne sensors in Lagrange 1 point (L1) and Geostationary (GEO) orbital configurations. Viewing from L1 and GEO orbits significantly augment target detection opportunities in relation to those

resulting from traditional low earth orbit (LEO) satellite observations. GEO observations provide more viewing opportunities of a fixed region on Earth at fine temporal and spatial resolutions (Jing et al., 2024), whereas L1 observations allow multiple observations of the entire rotating Sunlit disk of the Earth to achieve global coverage in a single day. The availability of daytime near-hourly aerosol measurements from L1 and GEO vantage viewing points enables the continuous real time monitoring of the atmosphere and also contributes to improving modelling capabilities by enabling the validation of simulation experiments of short time scale physical processes.

Since 2020, a constellation of high-resolution GEO spectrometers has been deployed to monitor the concentration of important air quality (AQ) relevant trace gases (tropospheric O₃, NO2, and others) as well as tropospheric aerosols. The Korean Geostationary Environment Monitoring Spectrometer (GEMS) sensor (Kim et al., 2020; Kim et al., 2018) on the GEOKOMPSAT-2B satellite was launched in February 2020. GEMS field or regard goes from 5°S to 45°N and extends from 75° E to 145° E, covering of most of India, and the totality of Korea and Japan. More recently, the TEMPO (Tropospheric Emissions: Monitoring of Pollution) instrument (Zoogman et al., 2017), operated by National Aeronautics and Space Administration (NASA), on the GEO Intelsat-40 telecommunications platform, was deployed in April 2023. With a field of regard going from 25°N to 60°N and from 80°W to 115°W, the TEMPO sensor is intended to monitor AQ over the continental United States, parts of Canada, and Northern Mexico. The third component of the AQ GEO-ring of sensors is European Space Agency (ESA)'s Sentinel-4 mission UV-VIS-Near-IR (UVN) spectrometer onboard the Meteosat Third Generation satellite (MTG-S1) launched in July 2025. UVN's geographical coverage from 30°N to 65°N and from 30°W to 45°E is intended to monitor AQ over Europe. The AQ GEO satellite constellation allows hourly aerosol load monitoring over the densely populated northern hemisphere (NH) regions. Except for GEMS, whose coverage extends to 5°S, the TEMPO and UVN sensors are designed exclusively for Northern Hemisphere (NH) extra-tropical coverage.

GEO-like global daytime multi-hourly observations of aerosols over the entire Sunlit disk of the Earth are also obtained from radiance measurements from the L1 vantage point by NASA's Aeronautics Space Administration) Polychromatic Imaging Camera (EPIC), on the Deep Space Climate Observatory (DSCOVR) satellite (Marshak et al., 2018). The DSCOVR spacecraft, operated by the National Oceanic and Atmospheric Administration (NOAA), was launched 11 February 2015, and reached its final L1 point destination, 1.5 million km towards the Sun, in early June 2015. EPIC is a UV-to-Near-IR 10-channel sensor designed to retrieve multiple atmospheric composition products including total column and tropospheric ozone, sulphur dioxide, as well as aerosols and cloud properties (Marshak et al., 2018). Except for a 7-month hiatus (July 2019 through February 2020), during which the instrument was held in safe mode, EPIC has operated nearly flawlessly since its June 2015 first light. EPIC's GEO-like multihourly measurements fill the observational gap over the tropics and southern hemisphere regions of the world not observed by spaceborne sensors currently deployed on the GEO satellite fleet.

In this paper, published as part of a collection of articles on the 10th anniversary of the launch of the DSCOVR mission, we discuss in detail the decadal EPIC near UV aerosol record, formally named as the EPICAERUV aerosol product. In section 2, we describe recent algorithm upgrades that enhance the accuracy of retrieved aerosol optical depth (AOD), single scattering albedo (SSA), and above-cloud AOD (ACAOD). In section 3, we discuss a decade-long record of EPIC near UV aerosol data in all-sky conditions (i.e., cloud-free and above-cloud). Section 4 describes major mesoscale aerosol events in different regions around the world associated with the occurrence of biomass burning, wildfires, and dust storms. The paper is summarized and concluded in section 5.

2 EPIC near UV aerosol algorithm

As with the TOMS (Total Ozone Mapping Spectrometer) and OMI (Ozone Monitoring Instrument) heritage algorithms (Torres et al., 2020; Torres et al., 2012), the EPIC near UV inversion algorithm (EPICAERUV) uses pre-calculated radiance look-up tables (LUT's) for assumed aerosol particle size distributions and real component of the refractive index (Torres and Ahn, 2024). Surface reflectance in the near UV is characterized by making use of climatological data sets based upon minimum Lambertian Equivalent Reflectivity (LER) derived from heritage instruments (Herman and Celarier, 1997).

The original EPICAERUV algorithm (v.0.5.0.0) used observations at 340 nm and 388 nm to derive near UV aerosol optical depth (AOD) and single scattering albedo (SSA) at the longer wavelength. SSA values at 340 and 500 nm, also reported, were calculated using the implicit Aerosol Absorption Exponent (AAE) in the LUT's. Because of the known dependence of retrieved AOD and SSA parameters on aerosol layer height (ALH), the initial EPICAERUV algorithm relied on ALH assumptions based on either model calculations or climatological data bases constructed from space-borne CALIPSO lidar observations as in the heritage algorithms (Torres and Remer, 2013). Relevant upgrades to the current EPICAERUV algorithm (v.0.6.4.8) are described in this section.

2.1 UV-visible multi-spectral single scattering albedo

An important upgrade to the current EPICAERUV algorithm is the conversion of retrieved 388 nm SSA to 354, 440, 500, and 646 nm. The conversion is carried out using a quadratic fit approach pivoted to the retrieved SSA at 388 nm to report the spectral SSA at the listed additional wavelengths. The quadratic fit approach relies on a research data set developed using long-term AERONET-OMI-MODIS synergy observations to derive SSA at the UV (OMI) and visible (MODIS) wavelengths independently without any prior assumptions on the spectral dependence of aerosol absorption (Kayetha et al., 2022). To capture the variability in aerosol absorption, the research dataset was first categorized, based on 110 globally distributed AERONET sites, into three prevalence aerosol type environments of carbonaceous aerosols, mineral dust, and urban-industrial. The identified regions with the

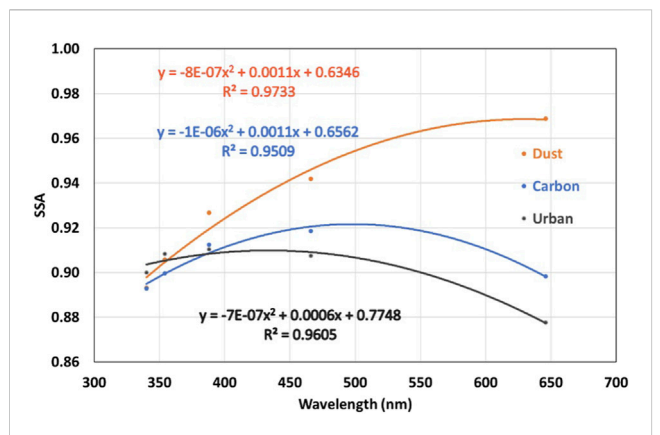


FIGURE 1
Near-UV to visible spectral dependence of SSA for the three major aerosol types (dust, carbonaceous aerosols, and urbanindustrial) representing JJA period for Sahara, Sahel, and all urban location average deduced from the work of Kayetha et al. (2022). The derived coefficients of polynomials for the respective aerosol types are included in the plot.

seasonal presence of carbonaceous aerosols include Sahel, Southern Africa, Middle East, Eastern China, Northern India, Australia, United States, and South America. Those for the mineral dust aerosol types include Sahara, Middle East, Eastern China, and Northern India. The urban-industrial aerosols are represented with an averaged spectral SSA model derived from all urban locations considered in the study. The spectral SSA polynomials for areas outside these pre-defined regions are represented with the default models for the three respective aerosol types, i.e., USA-South America averaged polynomials for carbonaceous smoke, Saharan desert spectral SSA for dust, and all urban location average for the urban-industrial aerosol types. The polynomial coefficients are then used to estimate the aerosol SSA at 354, 388, 440, 500 and 646 nm following an offset adjustment (retrieved minus estimated SSA) based upon the SSA retrieval at the reference wavelength of 388 nm.

Figure 1 shows the polynomial expressions derived for the Sahel region for carbonaceous, mineral dust for Saharan desert, and averaged urban-industrial aerosols during the JJA period. Figure 2 displays example maps of the retrieved SSA at 388 nm from near-UV aerosol algorithm on 18 June 2020 (16:30 UTC) and reported spectral SSA at 440, 500, and 646 nm using the quadratic fit approach.

2.2 Above-cloud aerosol optical depth (ACAOD)

Another major EPICAERUV improvement was the implementation of above-cloud aerosol optical depth (ACAOD) retrieval to account for the presence of either smoke or desert dust layers found above cloud decks. The inversion approach was developed using OMI near UV observations (Torres et al., 2012). It simultaneously derives ACAOD along with the actual cloud optical depth (COD), or aerosol-corrected COD, after accounting for aerosol absorption effects. A similar approach was subsequently applied to MODIS visible observations (Jethva et al., 2013; Meyer et al., 2015).

Because of their absorption properties, carbonaceous particles generated from either biomass burning or wildfires, and windblown mineral dust above clouds can significantly enhance absorption effects in the atmosphere, influencing atmospheric stability, cloud lifetime and properties, and ultimately affecting the radiation balance (Seinfeld et al., 2016). Thus, accurate knowledge of the atmospheric aerosol load above clouds is needed for a better understanding of aerosol-cloud interaction processes generally referred to as direct, semi-direct, and indirect effects. The 10-year EPICAERUV ACAOD record extends the nearly two-decade long global ACAOD product from OMI observations (Jethva et al., 2013).

Evaluations of EPICAERUV-retrieved AOD, SSA, and ACAOD products by comparison to independent ground-based and airborne measurements have been carried out in a previous study (Ahn et al.,

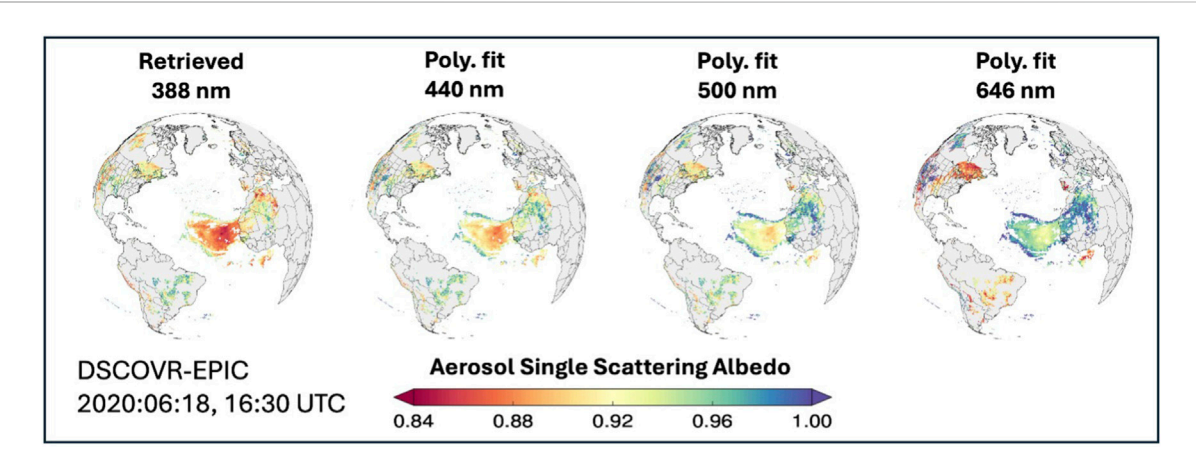


FIGURE 2
A case study example of converted SSAs at the visible wavelengths(440, 500, 646 nm) from the EPIC-retrieved SSA at 388 nm using the regional and seasonal polynomials demonstrated in Figure 1. Two distinct aerosol events are captured in this case study: 1) Saharan dust transport over the Atlantic Ocean showing increase in the spectral SSA at longer wavelengths, and 2) wildfire generated smoke in North America exhibiting increasing trend in SSA at the visible wavelengths.

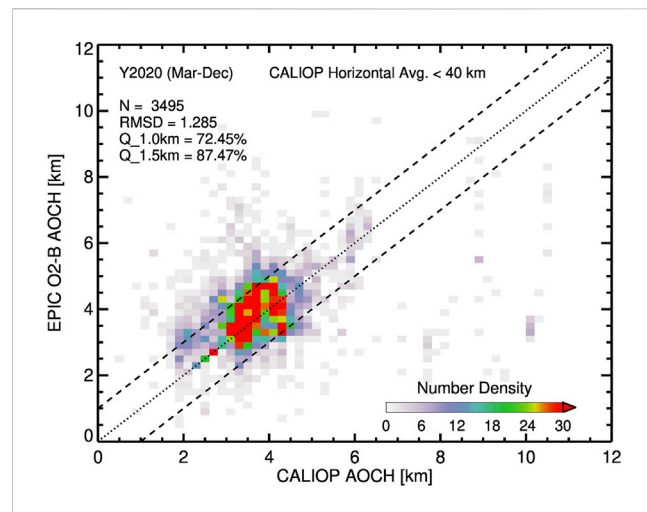


FIGURE 3 Global comparison of AOCH retrieved by EPIC Oxygen-B band and that calculated from CALIOP observations. The spacetime collocated dataset collected for the period March through December 2020 are used. RMSD: root-mean-square-difference, Q_1.0 km and Q_1.5 km are the percentage of total matchups contained within ± 1.0 km and ± 1.5 km agreement.

2021). The validation of the EPIC daily mean AOD values against that from AERONET at eight selected representative sites yields correlation coefficients in the range from 0.68 to 0.89 and root mean square errors in the range 0.10–0.31. A similar comparison of EPIC-retrieved SSA against the AERONET inverted SSA product revealed nearly 51% (76%) of matchups in agreement within ±0.03 (±0.05) differences. The EPIC-retrieved ACAOD are also found to compare reasonably well, with 50%–70% of matchups falling within the expected uncertainty against the direct airborne measurements acquired from HSRL-2 lidar and 4STAR sun photometer operated during the ORACLES field campaign in the Southeastern Atlantic Ocean. Subsequently, the diurnal variability in AOD and SSA using the EPICAERUV product has also been recently examined (Torres and Ahn, 2024).

2.3 Aerosol layer height

In the improved version of the EPICAERUV algorithm ALH assumptions are no longer required over the oceans and most land surface types. The enhanced algorithm introduces the retrieval of ALH using Oxygen-B band observations. Xu et al. (2017) Xu et al. (2019) have shown that effective ALH can be retrieved from observations at EPIC Oxygen-A (764 nm and 780 nm) and Oxygen-B (680 nm and 688 nm) bands. The remote sensing technique that utilizes observations in these bands has been shown to be effective in retrieving the aerosol optical centroid height (AOCH) of aerosol layers from EPIC observations (Xu et al., 2019). While both the Oxygen- A and -B bands can be used to retrieve AOCH over water surfaces, the larger land surface albedo and the associated uncertainties with the Oxygen-A band range make its application over land more challenging than that of the Oxygen-B band. Thus, in EPICAERUV, the 680-688 nm Oxygen-B band pair is used for retrieving AOCH which is assumed to represent the effective ALH of either carbonaceous or mineral dust aerosol layers over both water and most land backgrounds. Over bright desert areas, however, retrieving AOCH becomes more challenging. Therefore, the retrieval of near UV AOD and SSA over bright deserts and other instances when Oxygen-B band algorithm fails to retrieve ALH, still relies on a CALIOP-based ALH climatology developed over a decade ago for use in the OMI UV aerosol algorithm (Torres and Remer, 2013).

A comparison of EPIC Oxygen-B band derived AOCH to CALIOP-based ALH determination was carried out. The CALIOP-based ALH represents Level 1 backscatter-weighted aerosol layer height between the aerosol top and bottom altitudes identified in the Level 2 product. The comparison shows that in about 80% of collocated matchups, derived ALH by the two approaches agree within ±1 km for specific smoke and dust events. Globally, as shown in Figure 3, the collocated ALH datasets calculated from both sensors for the period March through December of 2020 are found to agree with each other for ~72% and 87% of matchups within ±1 km and ±1.5 km differences, respectively. These results support the use of EPIC Oxygen-B band ALH retrievals as a reliable way to prescribe ALH for the accurate determination of AOD and SSA from near UV observations. The reprocessed EPICAERUV global aerosol dataset is freely accessible at NASA's Atmospheric Science Data Center (ASDC) at the URL: https://asdc.larc.nasa.gov/project/ DSCOVR/DSCOVR_EPIC_L2_AER_03 (NASA/LARC/SD/ASDC, 2019).

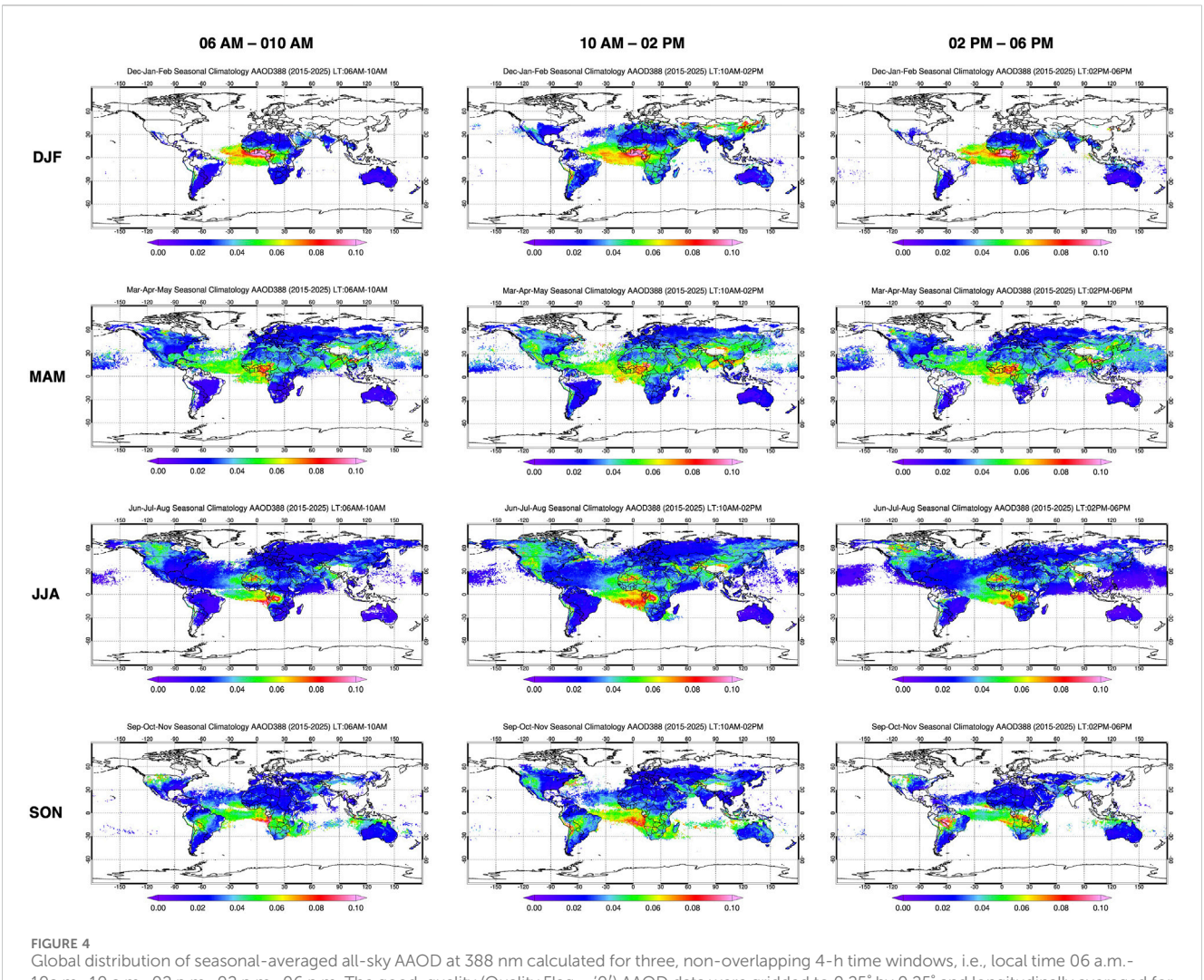
3 The EPICAERUV decadal record

3.1 Seasonal climatology of aerosol absorption optical depth

The 10-year EPICAERUV aerosol product further extends the multi-decade long global record of near-UV AOD and SSA, along with the UV Aerosol Index (UVAI), initiated by the TOMS (Total Ozone Mapping Spectrometer) sensors on the Nimbus-7 and Earth Probe satellites in the past century (Torres et al., 2012), and continued to the present by the Ozone Monitoring Instrument (OMI) on the Aura platform (Torres et al., 2020; Ahn et al., 2008) and the TROPOspheric Monitoring Instrument (TROPOMI) on the Sentinel5-Precursor satellite (Torres et al., 2020).

Large scale smoke plumes generated by tropical biomass burning events (Rogers and Bowman, 2001) and by extra-tropical wildfires, and other massive aerosol plumes that once were considered rare events such as the Yellowstone Park fires (Romme and Despain, 1989) and the great China fires in the late 1980s, as well as the optically thick smoke plume associated with the 1991 Gulf war (Torres and Remer, 2013), have, in recent years, become seasonal synoptic scale events affecting huge regions over thousands of square kilometers, frequently degrading regional air quality, disrupting economic activities such as large-scale agriculture and commercial aviation operations.

The EPICAERUV record covers the 2015–2025 decade, a period when significant increases in the frequency of wildfires at mid and high latitudes have taken place. Carbonaceous aerosols that



Global distribution of seasonal-averaged all-sky AAOD at 388 nm calculated for three, non-overlapping 4-h time windows, i.e., local time 06 a.m.-10a.m., 10 a.m.-02 p.m., 02 p.m.-06 p.m. The good-quality (Quality Flag = '0') AAOD data were gridded to 0.25° by 0.25° and longitudinally averaged for each latitude grid.

traditionally had been associated with agriculture-related activities such as waste disposal and forest clearing, mostly in tropical and subtropical regions of the world, are now routinely observed at mid and high latitudes in both hemispheres. Thus, what was traditionally an agriculture-related phenomenon, has turned into an environmental global issue as wildfires have become common occurrence events in Canada (Jain et al., 2024) and the United States (Balch et al., 2024), Europe and Russia (Yasunari et al., 2024), in the northern hemisphere, and in the extra-tropical regions in the Southern Hemisphere such as Australia (Clarke et al., 2022), Southern Chile (Cordero et al., 2024), and Argentina.

Figure 4 shows global maps of 10-year seasonal averages of EPIC-retrieved all-sky AAOD at 388 nm. The AAOD data was further averaged over three 4-h time windows representative of local morning (6 a.m.-10 a.m., left panel), late morning to early afternoon (10 a.m.-2 p.m., center) and afternoon (2 p.m.-6 p.m.) prevailing meteorological conditions. The AAOD maps are shown for four northern hemisphere seasons, i.e., winter (December-January-February, first row), spring (March-April-May: 2nd row), summer (June-July-August: 3rd row), and fall (September-October-

November: 4th row). A brief description of obtained climatological maps is presented here.

The most active aerosol source during the northern hemisphere winter season (DJF) is equatorial Africa where biomass burning activities generate large atmospheric loads of carbonaceous aerosols. Largest AAOD values are observed over western equatorial Africa in all three time-windows. The spatial extent of the aerosol plume over the ocean, however, is slightly reduced in the morning observations in relation to the near-noon and afternoon retrievals. A plume of lower AAOD over the Atlantic Ocean in the near-noon depiction is likely associated with aerosols above clouds. Another aerosol source is present over the near-noon time window over East Asia, which is likely related to the wintertime biomass burning.

The observed AAOD geographical distribution during the Spring season shows two major aerosol plumes originating in Equatorial and Northern Africa that are present over the Atlantic Ocean. The largest northernmost plume extending east-to-west is associated with mineral aerosols blown off the Saharan desert, while the southernmost plume off the coast of Equatorial Africa is mostly made of carbonaceous aerosols. The dust plume shape does not

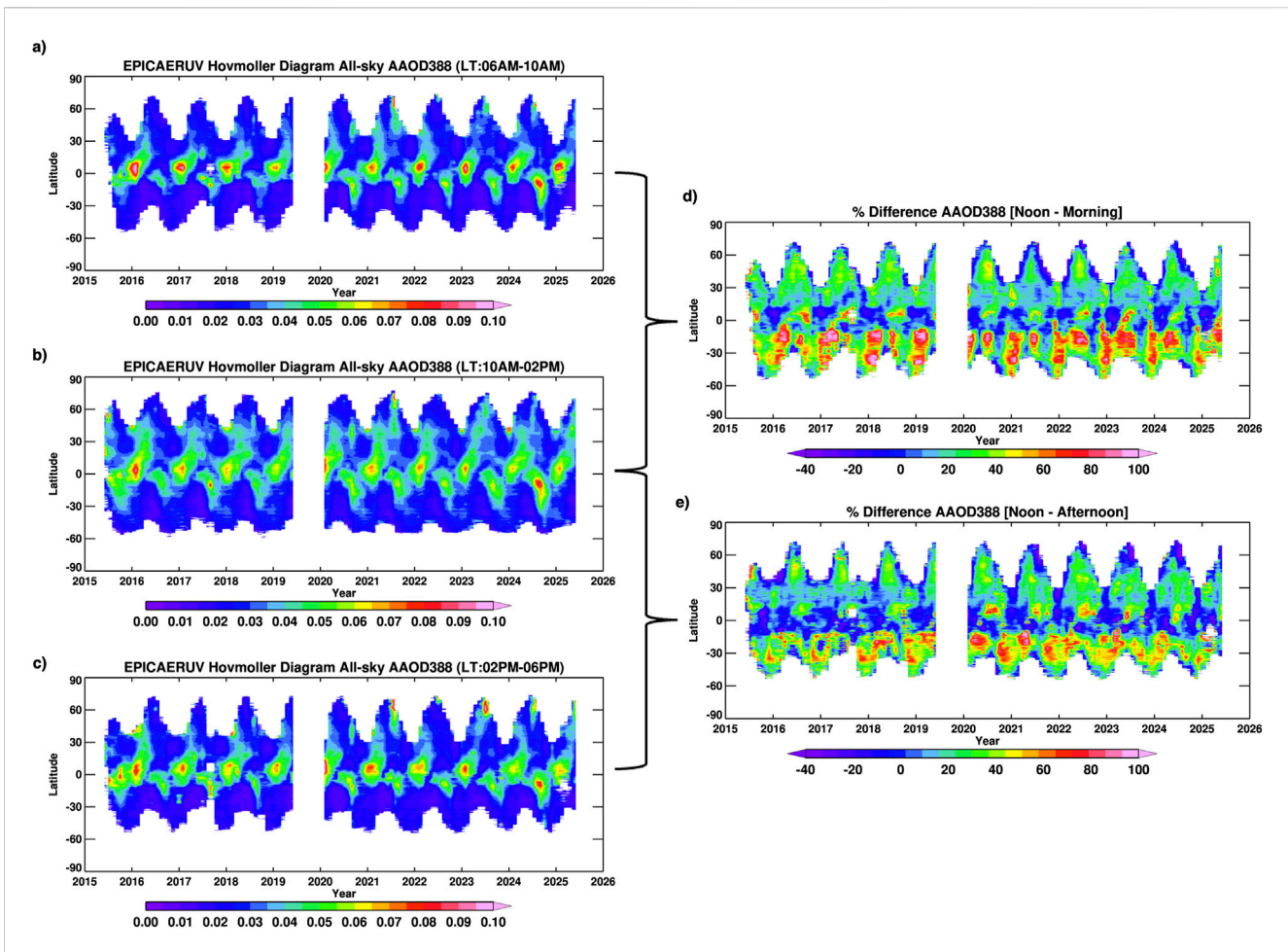


FIGURE 5
Howmöller diagrams of the EPICAERUV all-sky AAOD retrieved at 388 nm for the three different local time frames, i.e., (a) 6 a.m.-10a.m., (b) 10 a.m.-2 p.m., and (c) 2p.m.-6 p.m. The AAOD data were gridded to 0.25° by 0.25° and longitudinally averaged for each latitude grid. Only good-quality (Quality Flag = '0') retrievals were used. The percent difference in AAOD at 388 nm between the around-noon and morning, and around-noon and afternoon time windows are shown in (d) and (e), respectively.

change significantly over the time-windows shown. The plume further south, likely appears less intense in the morning than it does in the noon and afternoon observations. Asian desert dust sources appear activated with comparable strengths over the three time-windows. Also, during this season large aerosol signals over Southeast Asia and over coastal regions of India are observed with a significantly stronger noon signal possibly associated with transported dust from Indian deserts (Li et al., 2019) mixed with the springtime agricultural burning in the southeastern states of India and Southeast Asia. The spatially extended aerosol signal over the mid-west and western United States is possibly the result of both desert dust and carbonaceous aerosols. The aerosol signal spread further north into Western Canada is likely associated with what is now becoming an early onset of the wildfire season. The noon view shows a significantly larger spatial extent of the plumes than those in the morning and afternoon representations.

The NH summer season global aerosol distribution is largely dominated by the presence of wildfire generated carbonaceous aerosols over North America and Siberia. Over both these regions, the spatial distributions of the aerosol plumes are largest

around noon. The Saharan dust plume over Western Africa and the Atlantic Ocean shows little variability over the course of the day. The most prominent Southern Hemisphere aerosol signal corresponds to carbonaceous aerosols from biomass burning in sub-tropical Africa with an aerosol signal significantly larger in the near-noon observations that those during the morning and afternoon timewindows consistent with previously reported estimates (Giglio, 2007; Mu et al., 2011).

The EPIC fall time (SON) maps of aerosol spatial distribution are shown in the bottom row of Figure 4. Southern African sources of biomass burning aerosols are fully activated with the southward shift of the burning belt to further southeastern areas of the continent (Eck et al., 2013). A westward moving plume over the South Atlantic overlie semi-permanent, low-level stratocumulus clouds, which is well-resolved in the ACAOD product of EPICAERUV. Plume intensity is largest at noon and reduced in the morning and afternoon. The transport of dust across the Atlantic is also apparent.

Fire activity over Indonesia can also be seen during this season (Field et al., 2016). The smoke signal over South America is clearly

observed in the morning and near-noon depictions but it is significantly stronger in the afternoon hours. The observed eastward smoke mobilization across the Atlantic Ocean is observed in both the noon and afternoon windows.

3.2 Hovmöller diagrams: decade-long timeseries of aerosol absorption optical depth

Hovmöller diagrams in Figures 5a-c illustrate the diurnal variability of EPICAERUV derived global 388-nm AAOD in allsky conditions. Zonally-averaged AAOD in three time-windows: morning (top), around-noon (middle), and afternoon (bottom) representative of the local diurnal cycle are shown. Although the reported results include both carbonaceous and desert dust aerosols, the carbonaceous aerosol load is clearly the dominant component, especially over the northern latitudes. As expected, largest AAOD values are observed in the tropics and sub-tropics where most agriculture-related biomass burning takes place. The AAOD signature of wildfires can clearly be observed in both the morning and near-noon time windows. The near-noon depiction, however, shows significantly larger AAOD values extending to 60°N. The last 3 years of the shown EPICAERUV record depicts the wildfire AAOD signature extending further north than in the earlier part of the record, indicating the increasing severity and spread of the wildfire-generated smoke plume in northern hemisphere. The percent difference in AAOD between aroundnoon minus morning and around-noon minus late-afternoon time windows, as shown in Figures 5d,e, respectively, reveal a striking difference of as large as 80% in southern hemisphere, around 30°S latitude, likely associated with the continental biomass burning in South America and central/southern Africa. The diurnal differences of AAOD in the northern hemisphere, i.e., northward of 30°N, are noted in the range 20%-60%, indicating significantly increased signal of aerosol loading around noon hours.

The well-defined AAOD diurnal cycle with near-noon maxima resulting from EPIC observations is consistent with earlier regional analysis of Geostationary Operational Environmental Satellites (GOES) that used parameterizations of measured fire radiative power (FRP) to derive a measure of total atmospheric aerosol mass (Zhang et al., 2012) over specific regions. Similar analyses over extended regions were carried out using combined GEO and LEO observations (Li et al., 2019). More recently, the FRP-based approach has been fully integrated into the Multi-Scale Infrastructure for Chemistry and Aerosols Version0 (MUSICAv0) and tested during the FIREX-AQ (Fire Influence on Regional to Global Environments and Air Quality) WE-CAN (Western wildfire Experiment for Cloud chemistry, Aerosol absorption and Nitrogen) field campaigns (Tang et al., 2022). The observed consistency of resulting diurnal cycles of FRP-based parameterization of total carbonaceous aerosol mass and satellite derived AAOD of carbonaceous aerosols is not surprising. FRP and the carbon content of burning vegetation have a direct physical relationship as the released radiant energy is a direct consequence of the chemical oxidation of the fuel which is primarily composed of carbon (Seiler and Crutzen, 1980).

4 EPIC observed extraordinary aerosol events

In this section we briefly document mostly wildfire-related aerosol events that did not go unnoticed due to their severity in terms of the intensity of their effect on the atmosphere in addition to material losses. Although some of these events have been addressed in detail in the literature, we describe them in the context of the unique EPIC viewing capability in terms of chronological order.

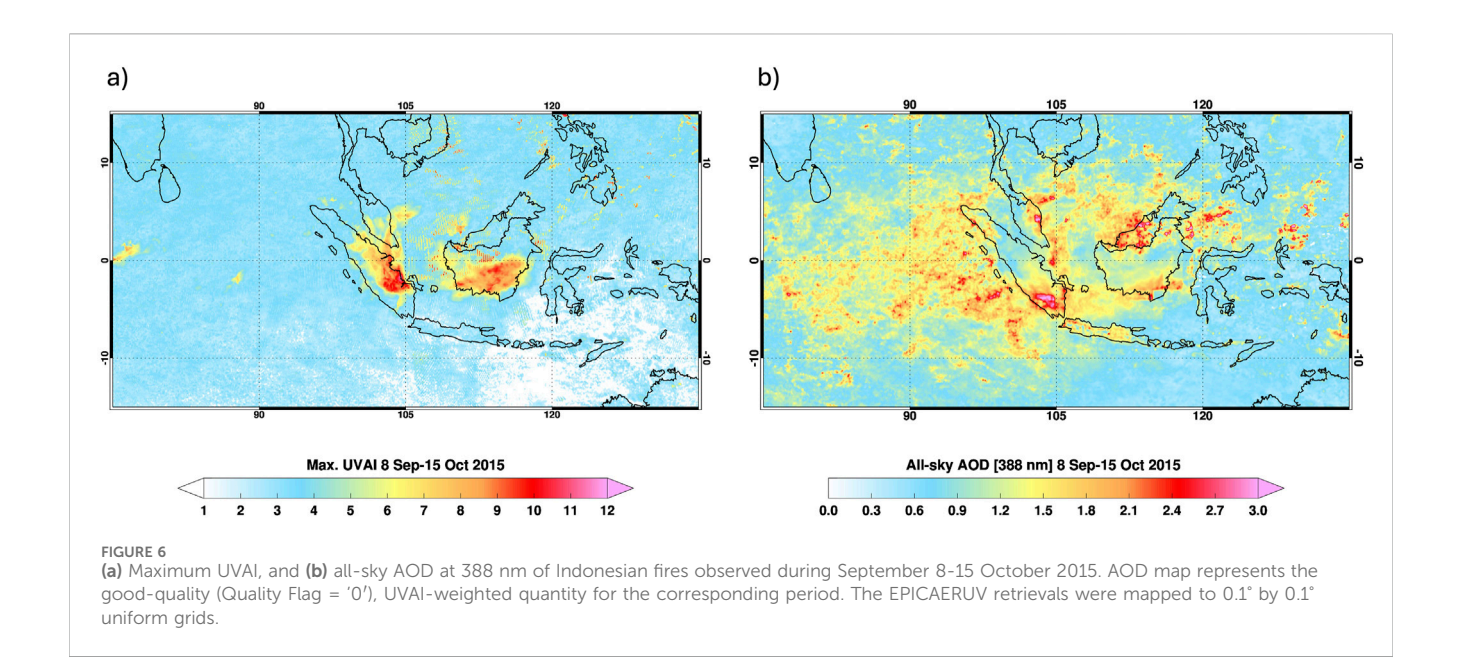
4.1 Unprecedented biomass burning aerosol load in Indonesia in 2015

During the September-October period in Indonesia, fires are typically started to dispose of logging and agricultural waste in preparation for the new growing season. Often the biomass burning runs out of control because of the prevailing meteorological conditions and associated drought over degraded peatland areas (Wang and Coauthors, 2024; Rein et al., 2008). The intensity of the fires is particularly strong during El Niño years when the burning of dried peat burning is most efficient (Page et al., 2002; Field et al., 2004). Fires have commonly been observed in Sumatra as early as in the 1960s (Field et al., 2009) and since the 1980s over Kalimatan and Borneo (Malingreau et al., 1985). The 1997 fire season in this region is regarded as the worst on record producing an optically thick plume that blanketed most of Southeast Asia. Ground-based measurements of multiple aerosol parameters, including spectral optical depth (AOD) and single scattering albedo (SSA), were carried out at the Kuala-Lumpur airport in 1997 (von Hoyningen-Huene et al., 1999). Since the deployment of the DSCOVR-EPIC observatory in early 2015, two large scale episodes in this region have occurred in 2015, and, most recently, in 2019. The 2019 event, however, was not observed by EPIC as the sensor had gone in safehold mode from July 2019 through March 2020. The 2015 Indonesian fire season has been described in detail by Field et al. (2016). It started in Sumatra in July followed by extensive fires in August in Kalimantan. It is estimated that about 2.6 million hectares of agriculture dedicated land burned (Field et al., 2016). By mid-September most of these regions were buried under a thick smoke layer. By October the smoke plume had further extended to Thailand, Malaysia and Singapore. AERONET observations at multiple locations in SE Asia reported 380 nm AOD larger than 3.

Figure 6 displays the spatial distribution of a) maximum UVAI values and b) UVAI-weighted temporally averaged all-sky AOD at 388 nm measured by EPIC between September 8 through 15 October 2015. The impact of the fires can be seen in these maps with enhanced values of UVAI (7–10) and AOD (up to 3.0) over Sumatra and Kalimantan. Larger AOD values far away from the source region and over the Indian Ocean have appeared to be affected by sub-pixel cloud contamination.

4.2 January 2017 Chilean megafires

Wildfires of unprecedented magnitude broke out in Southern-Central Chile in mid-December 2016, extending through early



February 2017, and more recently in 2023 (de Graaf et al., 2023). Nearly 5,200 square kilometers were destroyed, and twelve casualties were reported (Pliscoff et al., 2020) as consequence of the 2017 fires. A significant increase in the atmospheric aerosol load, in terms of aerosol optical depth, was detected by AERONET's observations at the Santiago_Beauchef site. Normally low background AOD values show a significant increase to near unity in mid-December 2016 and rising to above 1.0 on December 24. Further AOD increases took place in January 2017, reaching highest values, larger than 3, on January 18. Fire activity and elevated aerosol load continue throughout early February. An 11-day composite EPICAERUV retrieved maximum UVAI, and UVAI-weighted quantities of ALH, AOD, and SSA, as displayed in Figure 7, shows the spread of the aerosol plume toward the northwest direction over the South Atlantic Ocean. To create these maps, the EPICAERUV data for each timeframe were first gridded to 0.1° by 0.1°. The maximum UVAI value for each grid point was then extracted from the multiple timeframes covered in the given period. The time averaged cloudfree ALH and SSA and all-sky AOD were calculated by weighting the respective good quality retrievals with corresponding UVAI values. Weighing aerosol retrievals with UVAI, i.e., larger the UVAI greater the weight, in deriving multiday/week composites minimizes the effects of cloud contamination in clear sky conditions and provides more realistic representation of the magnitudes of aerosol events. This specific format was adopted for processing and creating maps for all aerosol events presented in this paper. UVAI values as large as 10 are observed at the plume's core (Figure 7a). Aerosol layer height values between 3 and 7 km are apparent (Figure 7b), whereas largest AOD values as large as 2 (Figure 7c) and SSA values around 0.90 (Figure 7d) are present at the plume's core.

4.3 The 2017 British Columbia fires

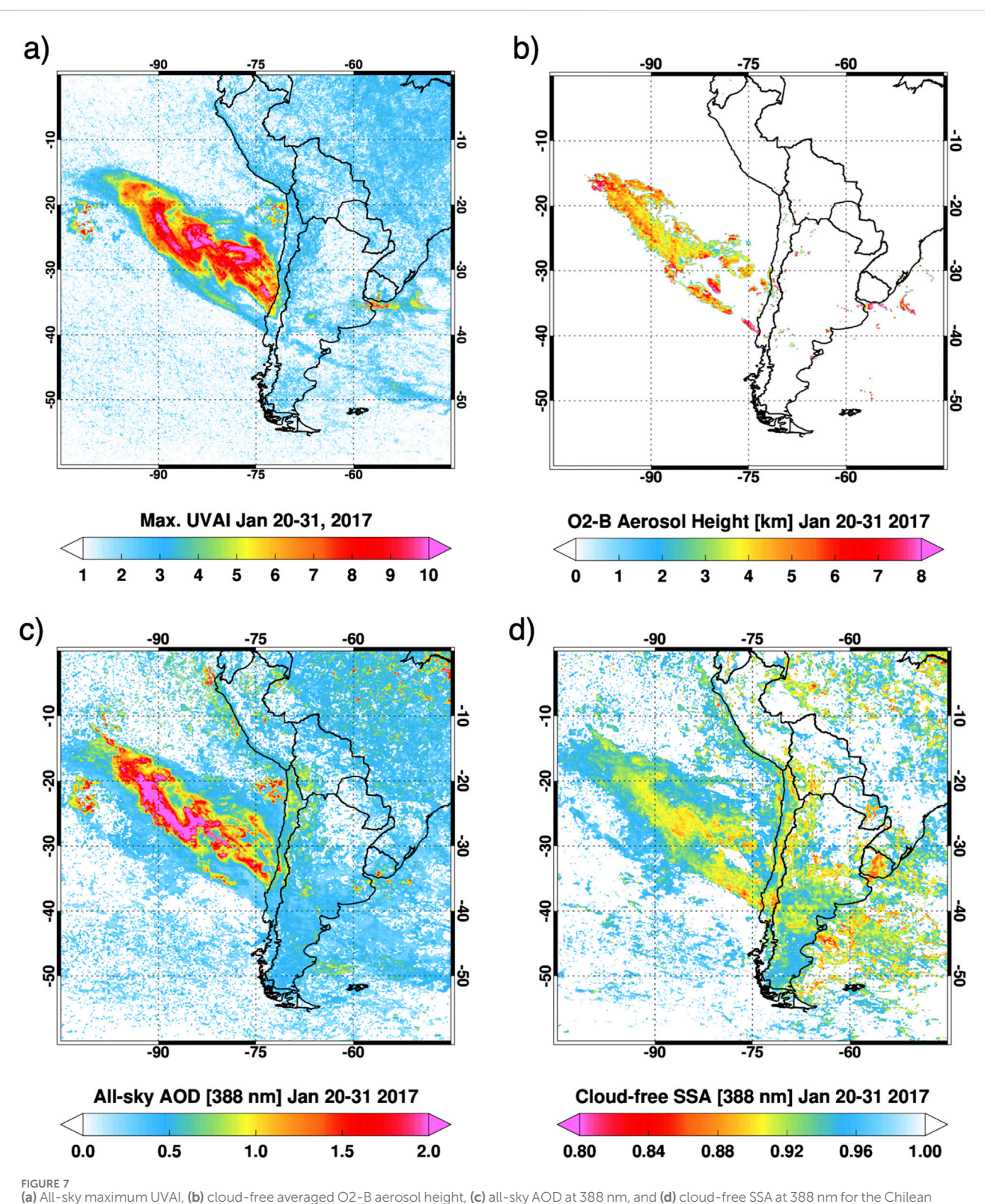
Wildfires in the Canadian British Columbia (BC) province in early August 2017 were identified by EPIC UVAI signal. This event

generated an optically thick carbonaceous aerosol layer that made its way to the lower stratosphere. EPIC multi-hourly daily observations monitored the spatial and temporal evolution of the plume for about 6 weeks. Using EPIC AOD retrievals in cloud-free skies, it was estimated that nearly one-10th of the estimated carbonaceous aerosol mass (268 Kt) reached the stratosphere on 13 August 2017, and the rest of the plume did so in the next few days (Torres et al., 2020).

Figure 8-left shows the spatial extent of the smoke plume in terms of maximum UVAI from EPIC observations over a 2-week period in August 2017. Figure 8-right shows the retrieved 388-nm AOD (x-axis) and observed UVAI (y-axis) on 15 August 2017, at 19: 46:49 UTC over the area shown in Figure 8-left. In this demonstration retrieval, the SSA was fixed at 0.900 and AOD and ALH were derived. Also shown is the calculated relationship between ALH (between 3 km and 18 km) and UVAI. These results show the overall spatial distribution of ALH over the analysis area, indicating three distinct aerosol layer heights at about 2 km, 8 km and 16 km. AOD values as high as about 12 are observed at the lowest and highest levels, whereas a few cases of even larger AOD's are reported between 6 km and 10 km. A detailed investigation of the August 2017 British Columbia wildfires and resulting PyroCb event in terms of the EPIC aerosol retrievals and stratospheric mass estimation is described in Torres et al. (2020).

4.4 The September 2020 United States West coast fires

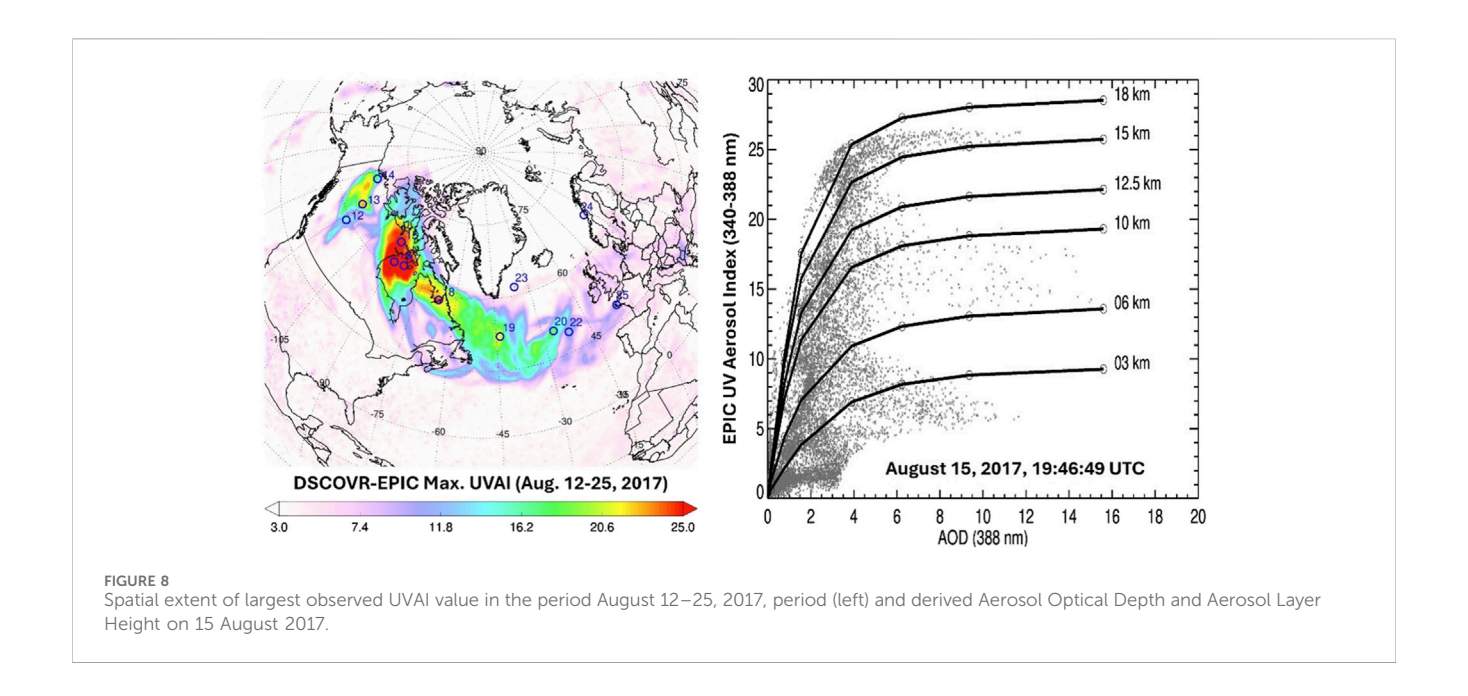
Unprecedented amounts of carbonaceous aerosols were produced by multiple fires over the United States west coast in September 2020. Continental scale smoke plumes from these wildfires were observed by the EPIC sensor for about 5 weeks since the onset of the fires in early September. Figure 9 shows that spatial coverage of the 2020 fires over the entire month of September in terms of EPIC observed maximum UVAI, and UVAI

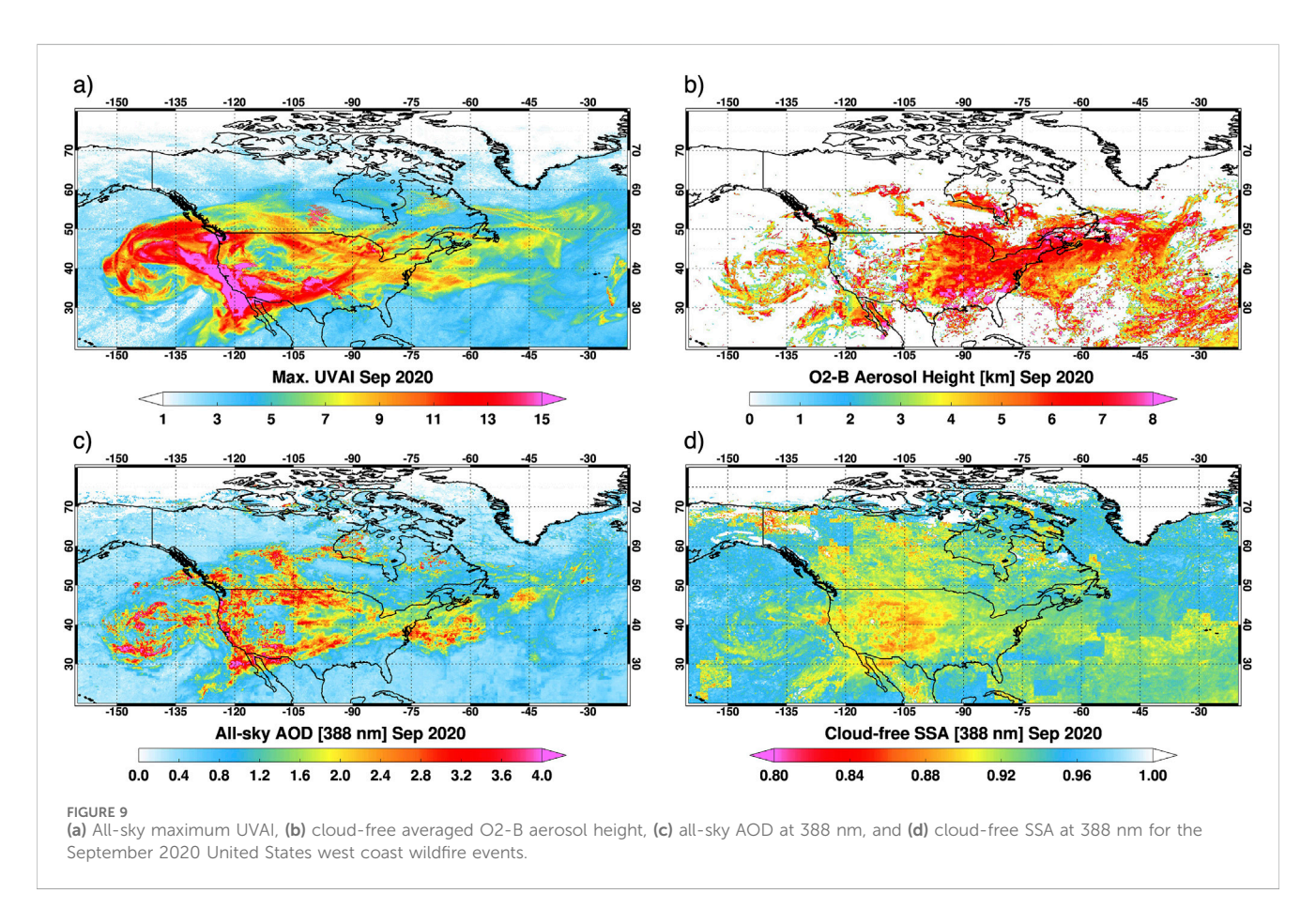


(a) All-sky maximum UVAI, (b) cloud-free averaged O2-B aerosol height, (c) all-sky AOD at 388 nm, and (d) cloud-free SSA at 388 nm for the Chilean wildfire event observed during January 20–31, 2017. Maps of the latter three parameters represent the good-quality (Quality Flag = '0'), UVAI-weighted quantities for the corresponding period. The EPICAERUV retrievals were mapped to 0.1° by 0.1° uniform grids.

weighted ALH, all-sky AOD, and cloud-free SSA. Massive amounts of emitted carbonaceous smoke aerosols produced UVAI signal as large as 15 and above along the west coast, which under the influence

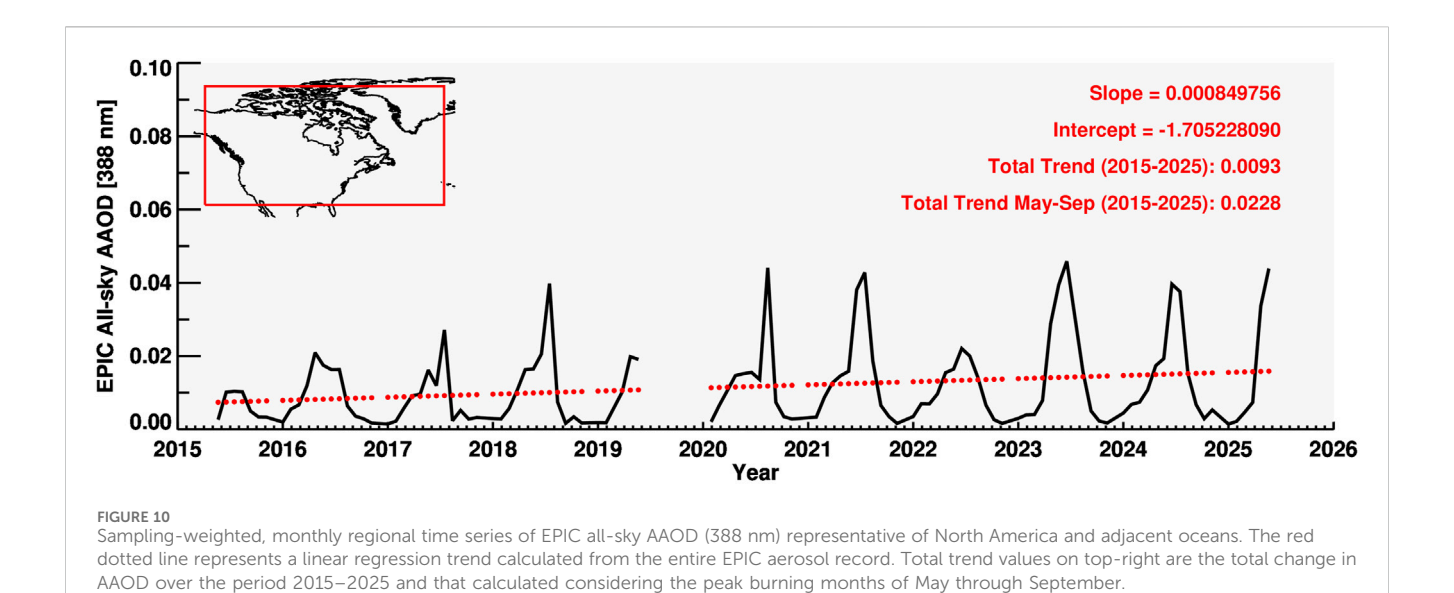
of prevailing winds were carried over in two opposite directions, one drifting over the Pacific Ocean and the other transporting eastward over the continental United States. All-sky AODs along these two





opposite transport pathways reached values as large as 3 and above, indicating significant smoke loading in the atmosphere. One of the most interesting observations of this intense smoke event is the spatial distribution Oxygen-B band retrieved ALH. Closer to the wildfire sources, the EPIC-retrieved ALH was noted relatively lower,

indicating smoke layers confined to lower levels of atmosphere (<3 km or so). On the other hand, the transported layers of smoke plumes over the eastern/northeastern parts of United States and the Atlantic Ocean are found to be elevated between the altitude range \sim 6–8 km, suggesting what appears to be a



dual effect of PyroCb generated updraft convective movements associated with uncontrolled and intense fires and the self-lofting mechanism fueled by strong absorption effects exerted by smoke aerosols (Torres et al., 2020; Ohneiser et al., 2023).

Although the 2020 United States west coast wildfire season was significantly more intense than in recent years, it is consistent with an increasing trend in fire frequency and intensity in this region observed over the last few years. We further investigate the longterm aerosol record using EPIC data, as shown in Figure 10, displaying a multi-year, regional time series of monthly mean allsky AAOD (388 nm) representative of North America and adjacent oceans. The monthly AAOD388 values were factorized (or normalized) using the total number of samples for each individual month relative to the maximum samples obtained for a specific month in the entire timeseries. Normalizing the monthly averaged value with the calculated sampling-based fraction ensures the representativeness of retrieval statistics over the chosen spatial and temporal domains. EPIC decadal record of aerosol absorption reveals a noticeable positive trend of ~0.00085 per year, translating to ~0.01 change in AAOD over 2015-2025 period. The spikes in AAOD during the late spring and summer months, especially for the latter half of the record, are associated with increased burden of carbonaceous aerosols produced by increasing frequency and intensity of wildfires in United States and Canada. The total trend value re-calculated for the peak burning season (May through September) shows a much larger increase in AAOD by ~0.023 during 2015–2025. A strong positive trend was also noticed in the total extinction AOD (not shown here) with an overall change of 0.1517 over the period 2015-2025 including all months and seasons, with even stronger change in AOD of ~0.37 during the peak burning period. In addition to casualties and economic losses, as well as deterioration of air quality in the vicinity of the fires, smoke plumes associated with fires in the Pacific Northwest have been found to reach the lower stratosphere (Peterson et al., 2018; Torres et al., 2020) where the residence time of carbonaceous aerosol particles is significantly longer, likely to result in climate effects.

4.5 June 2020 Northern Africa dust storm

The most intense Saharan dust storm ever observed took place during the June 13–27, 2020 period. It is believed to have been created by a series of haboobs generated as a result of intense convective activity over dust sources in West Africa (Marsham and Ryder, 2021). As discussed in detail by Yu et al. (2021), the elevated and optically thick aerosol layer, referred to as 'Godzilla' reached a 6–8 km altitude over the Atlantic Ocean, descending to about 4 km over the Caribbean Sea. Record high AOD values by both satellite-borne and ground-based instrumentation as well as record high PM_{2.5} concentrations over Puerto Rico were measured (Yu et al., 2021). Figure 11 displays the EPICAERUV composite aerosol retrievals derived using the observations from the entire month of June 2020.

4.6 East Asia dust storm in 2021

An unusually intense desert dust storm likely originated in northern China and southern Mongolia triggered a severe air quality deterioration over a wide area from northern China and extending eastward to the Korean Peninsula (Luo et al., 2022). Over the entire affected area, PM₁₀ concentrations significantly exceeded the regulated upper limit (150 µg/m³) reaching values higher than as large as 7,000 μg/m³ in Inner Mongolia and nearby provinces (Filonchyk, 2022). AERONET AOD measurements as high as 1.7 at the Gwanjiu_GIST site (35N, 127E) in Korea high as 1.7, possibly associated with this event, were observed on March 29. Similar observations at the Dalanzadgad site (44N, 104E) in Mongolia reported AOD's greater than 2.0 on March 15. Although these measurements are likely associated with the dust storm, AERONET assigned this data as level 1.0, indicating severe cloud contamination. Figure 12 displays the regional maps of the EPICAERUV aerosol retrievals focused over the Asian region showing the spatial extent of the dust plume over China and

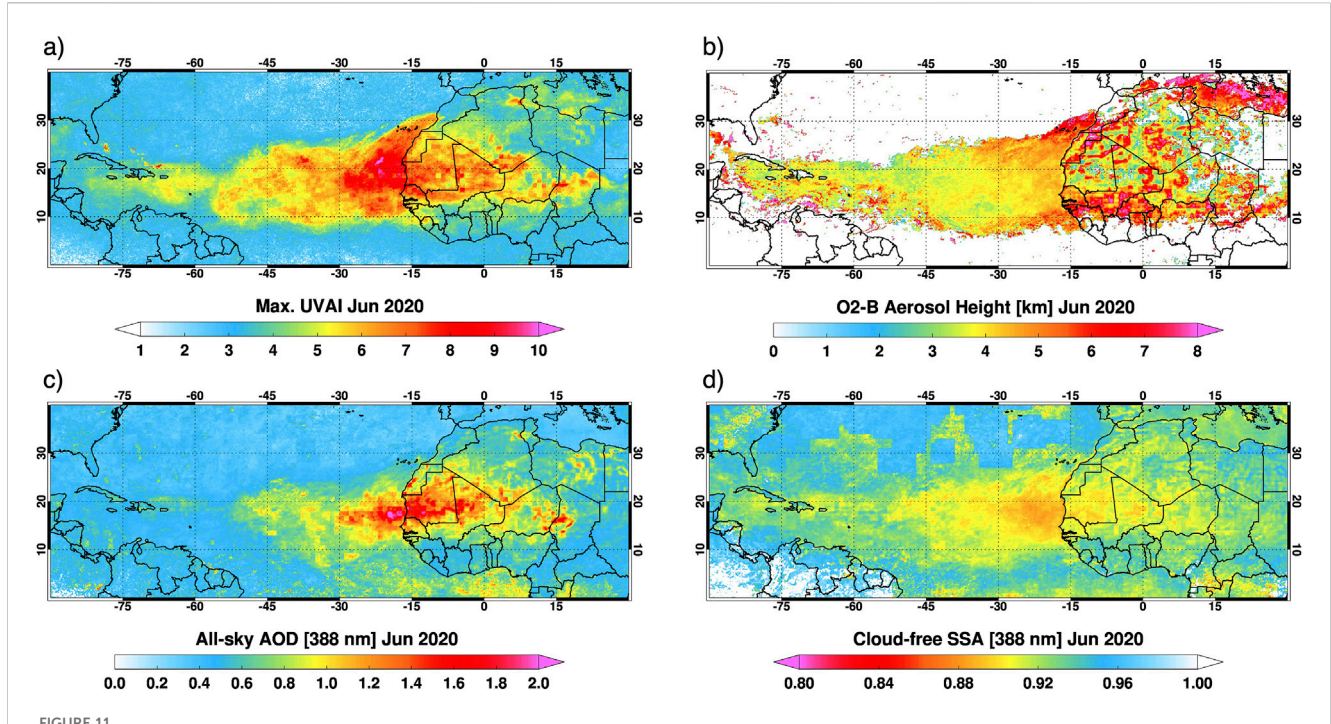
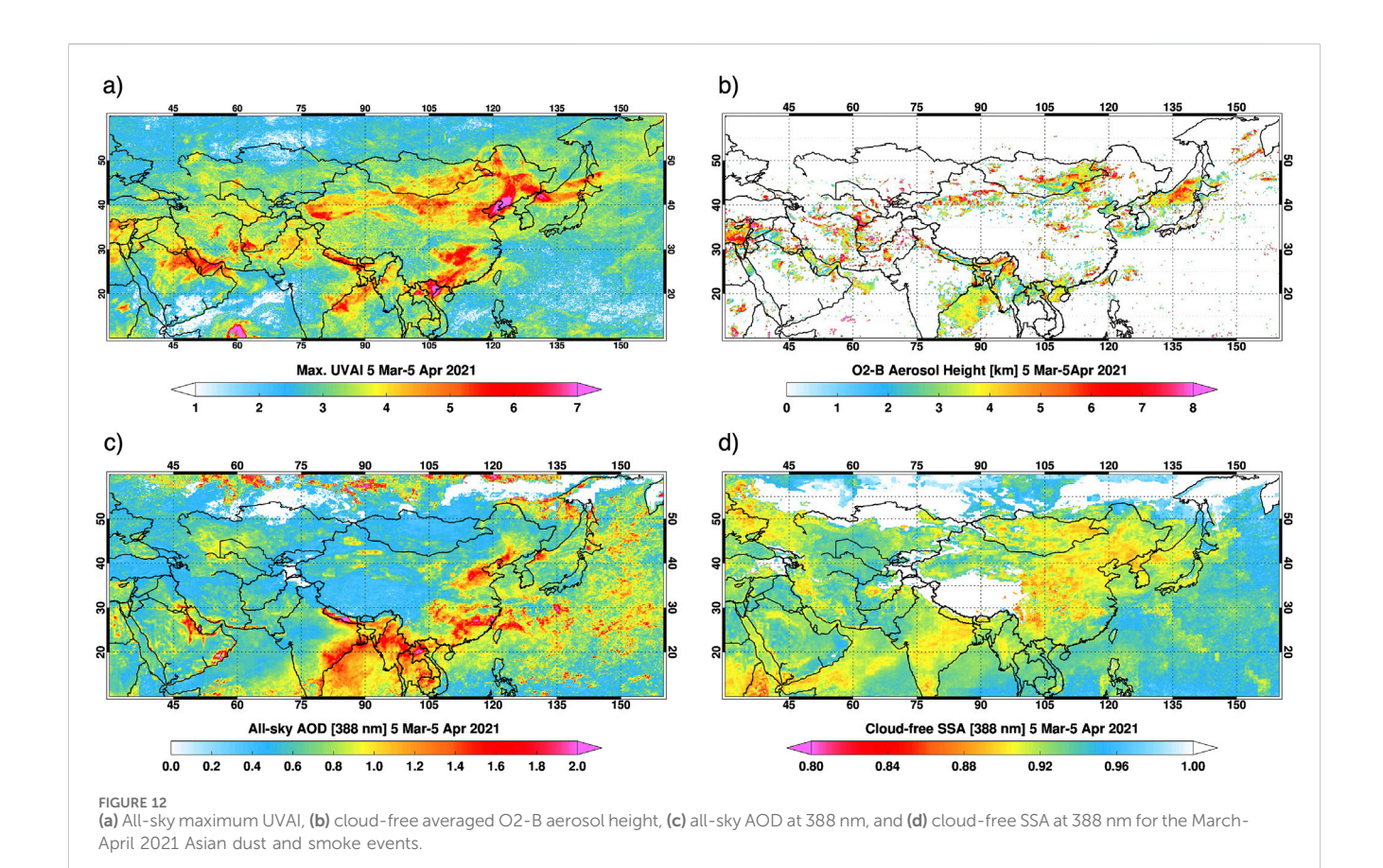
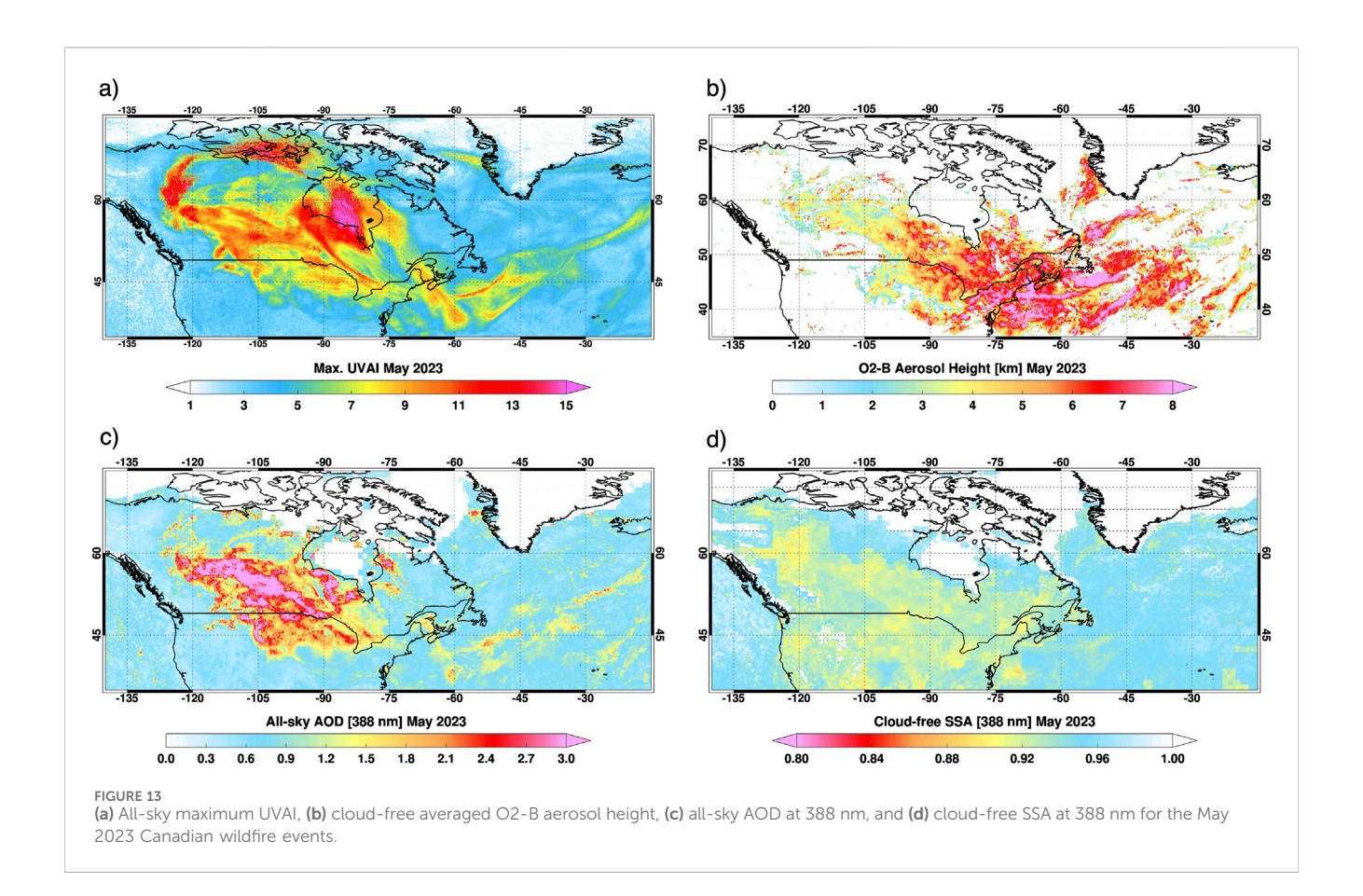


FIGURE 11
(a) All-sky maximum UVAI, (b) cloud-free averaged O2-B aerosol height, (c) all-sky AOD at 388 nm, and (d) cloud-free SSA at 388 nm for the June 2020 Saharan 'Godzilla' dust transport event.





Mongolia, and in the middle east region, wildfire-generated smoke loading over the foothills of Himalaya, and seasonal biomass burning aerosols over eastern India and Southeast Asia.

4.7 The 2023 fires in Canada

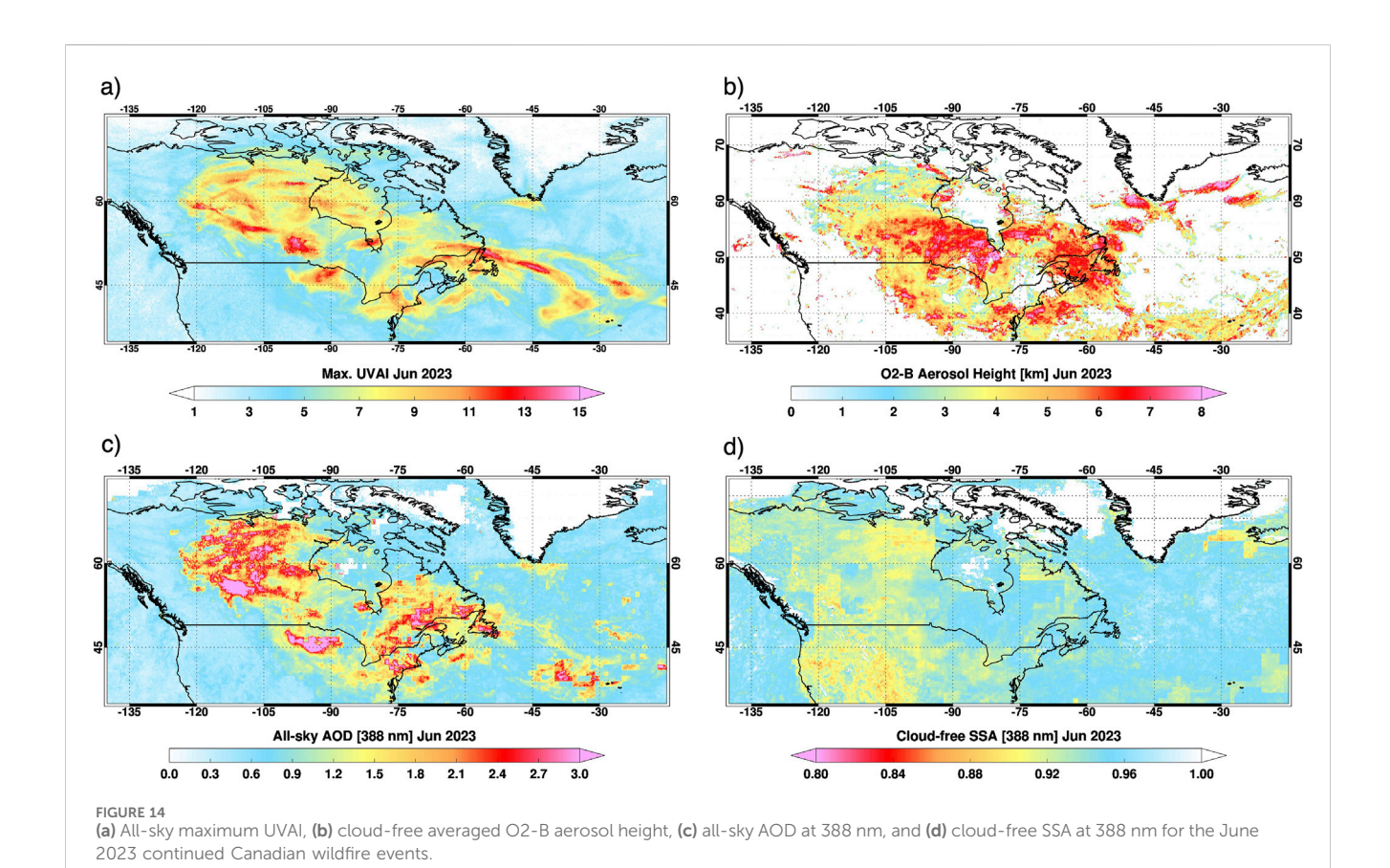
What is probably the most intense wildfire season on record over Canada took place during the summer of 2023. An estimated 15 million hectares (or about 4 times the area burned in 2017) were consumed by the 2023 fires. As a result of the fire activity not only was the atmospheric aerosol load significantly augmented, but also the concentration of carbon containing gases (Byrne et al., 2024), and other gaseous species directly emitted in the burning process or created by chemical interactions in the aftermath of the fires (Zhang et al., 2024). Because of the strong convective activity associated with wildfires it is suspected that a fraction of emitted carbonaceous particles may have reached the stratosphere as it happened in the 2017 British Columbia fires. Aerosols produced by the 2023 Canadian wildfire season were also horizontally advected to the South affecting the United States air quality (Chen et al., 2025) but also mobilized eastward across the Atlantic Ocean reaching western European cities with the implicit deterioration of air quality standards (Wang and Coauthors, 2024). Figures 13, 14 show the EPICAERUV aerosol data for the months of May and June 2023, respectively, neatly capturing the intensity and mobilization of smoke plumes over a much larger area. During the early burning season in Canada,

massive amounts of smoke aerosols emitted from wildfires spread over the length and breadth over Canada and north/northeastern United States, affected the air quality near source regions, however, mobilized eastward far away from the source region at higher altitudes of 6–8 km and beyond, as shown from the Oxygen-B band AOCH retrievals.

4.8 2024 fires in southern Brazil and Bolivia

The 2024 biomass burning in South America produced record amounts of carbonaceous aerosols. On 5 October 2024, 380 nm AOD of 3.7 was recorded at the AERONET Santa Cruz_UTEPSA site. This is the second largest AOD value ever measured at this site with a 20-year record, comparable to 2010 when an AOD of 3.5 was registered, and the second worst after the 2007 season when a record 4.6 value was recorded. Also unusual during the 2024 burning season in South America was the geographical location of the most intense fires in Bolivia, further south of Central Brazil where most of the burning usually takes place.

EPIC UVAI data on 5 September 2024, at 16:20:53 UTC (not included here but can be readily accessed at the URL: https://epic.gsfc.nasa.gov/aerosol?date=2024-09-05) shows the spread of the smoke plume over South America and the South Atlantic. The three-panel Figure 15 shows the plume spread in terms of UVAI (a), all-sky AOD (b), and ALH (c) maps derived from the entire month of September 2024.



All-sky AOD (288 nm) Sep 2024

FIGURE 15
(a) All-sky maximum UVAI, (b) all-sky AOD at 388 nm, and (c) cloud-free averaged O2-B aerosol height for the September 2024 biomass burning season in South America.

5 Summary and conclusion

The 2015–2025 decadal record of near UV aerosol optical depth and single scattering albedo, derived from L1 point observations by NASA's EPIC sensor on NOAA's DSCOVR spacecraft has been described. The latest improvement to the EPICAERUV algorithm used in this analysis, in relation to previously discussed results (Ahn et al., 2021; Torres and Ahn, 2024), is the derivation of aerosol layer

height from EPIC Oxygen-B band (680 nm and 688 nm) observations that significantly reduces the need of ALH assumptions based on external information, primarily for EPIC UVAI observations >2.0.

The unique advantage of L1 point viewing geometry, that combines the global spatial coverage capability of LEO observations with the diurnal cadence of GEO viewing, has been used to produce the first unique global multi-year record of GEO-

like near-UV aerosol properties. For simplicity, the discussion of long-term record has been carried out in terms of aerosol absorption optical depth that combines AOD and SSA into a single quantity.

The DSCOVR-EPICAERUV 10-year global and seasonal climatology illustrating the diurnal variability of the atmospheric aerosol load was discussed. To analyze the observed daytime cycle, the retrieved aerosol load information was grouped in three timewindows representative of morning, near-noon, and afternoon conditions. It was observed that the carbonaceous aerosol load resulting from biomass burning in the tropical and sub-tropical regions has a clearly discernable diurnal cycle. This effect was most clearly observed over the subtropics in South America, where significantly larger aerosol load during the SON months was observed in the noon and afternoon hours in relation to morning observations. Carbonaceous aerosol load associated with wildfire activity in North America is the most prominent carbonaceous aerosol feature shown in the EPICAERUV climatology.

The zonally averaged AAOD record clearly shows the AAOD trend captured by the EPIC UV aerosol record. The most interesting feature of this is the prominent AAOD increase at mid and high latitudes driven by the increasing wildfire activity over the last 7 years.

In the final section of the paper we presented brief descriptions of regional unprecedented aerosol events using EPIC aerosol dataset that made the news not only for their geophysical importance but also because of their impact on the quality of life and property damage of the affected communities.

Data availability statement

The datasets presented in this study can be found in online repositories. The names of the repository/repositories and accession number(s) can be found below: https://asdc.larc.nasa.gov/project/DSCOVR/DSCOVR_EPIC_L2_AER_03.

Author contributions

OT: Conceptualization, Funding acquisition, Investigation, Project administration, Supervision, Writing – original draft, Writing – review and editing. HJ: Data curation, Formal Analysis, Investigation, Methodology, Visualization, Writing – original draft, Writing – review and editing. CA: Investigation, Validation, Writing – review and editing. VK: Investigation, Visualization, Writing – review and editing.

References

Ahn, C., Torres, O., and Bhartia, P. K. (2008). Comparison of ozone monitoring instrument UV aerosol products with aqua/moderate resolution imaging spectroradiometer and multiangle imaging spectroradiometer observations in 2006. *J. Geophys. Res.* 113, D16S27. doi:10.1029/2007JD008832

Ahn, C., Torres, O., Jethva, H., Tiruchirapalli, R., and Huang, L.-K. (2021). Evaluation of aerosol properties observed by DSCOVR/EPIC instrument from the earth-sun lagrange 1 orbit. *J. Geophys. Res. Atmos.* 126 (12), e2020JD033651. doi:10.1029/2020JD033651

Balch, K., Iglesias, V., Mahood, A. L., Cook, M. C., Amaral, C., DeCastro, A., et al. (2024). The fastest-growing and most destructive fires in the US (2001 to 2020). *Science* 386, 425–431. doi:10.1126/science.adk5737

Funding

The author(s) declare that financial support was received for the research and/or publication of this article. This research was supported by the ROSES21-A.25 DSCOVR Science Team (Solicitation: NNH21ZDA001N-DSCOVR).

Acknowledgements

We thank the Principal Investigators (PIs) and staff of AERONET sites whose data was referred to in this work. We also acknowledge Marshall Sutton of EPIC team at NASA GSFC for processing the entire record of EPIC with the latest EPICAERUV algorithm.

Conflict of interest

Authors CA and VK were employed by Science Systems and Applications, Inc, funded by NASA.

The remaining authors declare that the research was conducted in the absence of any commercial or financial relationships that could be construed as a potential conflict of interest.

The handling editor AM declared a shared affiliation with the author OT at the time of review.

Generative AI statement

The author(s) declare that no Generative AI was used in the creation of this manuscript.

Any alternative text (alt text) provided alongside figures in this article has been generated by Frontiers with the support of artificial intelligence and reasonable efforts have been made to ensure accuracy, including review by the authors wherever possible. If you identify any issues, please contact us.

Publisher's note

All claims expressed in this article are solely those of the authors and do not necessarily represent those of their affiliated organizations, or those of the publisher, the editors and the reviewers. Any product that may be evaluated in this article, or claim that may be made by its manufacturer, is not guaranteed or endorsed by the publisher.

Byrne, B., Liu, J., Bowman, K. W., Pascolini-Campbell, M., Chatterjee, A., Pandey, S., et al. (2024). Carbon emissions from the 2023 Canadian wildfires. *Nature* 633, 835–839. doi:10.1038/s41586-024-07878-z

Chen, H., Zhang, W., and Sheng, L. (2025). Canadian record-breaking wildfires in 2023 and their impact on US air quality. *Atmos. Environ.* 342, 120941. doi:10.1016/j. atmosenv.2024.120941

Clarke, H., Cirulis, B., Penman, T., Price, O., Boer, M. M., and Bradstock, R. (2022). The 2019–2020 Australian forest fires are a harbinger of decreased prescribed burning effectiveness under rising extreme conditions. *Sci. Rep.* 12, 11871. doi:10.1038/s41598-022-15262-y

Cordero, R. R., Feron, S., Damiani, A., Carrasco, J., Karas, C., Wang, C., et al. (2024). Extreme fire weather in Chile driven by climate change and El Niño–Southern oscillation (ENSO). *Sci. Rep.* 14, 1974. doi:10.1038/s41598-024-52481-x

- de Graaf, M., Tilstra, L. G., and Stammes, P. (2023). Aerosol shortwave radiative heating and cooling by the 2017 and 2023 Chilean wildfire smoke plumes. *Geophys. Res. Lett.* 50, e2023GL104387. doi:10.1029/2023GL104387
- Eck, T. F., Holben, B. N., Reid, J. S., Mukelabai, M. M., Piketh, S. J., Torres, O., et al. (2013). A seasonal trend of single scattering albedo in southern African biomass-burning particles: Implications for satellite products and estimates of emissions for the world's largest biomass-burning source. *J. Geophys. Res.-Atmos.* 118, 6414–6432. doi:10.1002/jgrd.50500
- Field, R., Wang, Y., and Roswintiarti, O. (2004). A drought-based predictor of recent haze events in western Indonesia. *Atmos. Environ.* 38 (13), 1869–1878. doi:10.1016/j. atmosenv.2004.01.011
- Field, R. D., van der Werf, G. R., and Shen, S. S. P. (2009). Human amplification of drought-induced biomass burning in Indonesia since 1960. *Nat. Geosci.* 2 (3), 185–188. doi:10.1038/ngeo443
- Field, R. D., van der Werf, G. R., Fanin, T., Fetzer, E. J., Fuller, R., Jethva, H., et al. (2016). "Indonesian fire activity and smoke pollution in 2015 show persistent nonlinear sensitivity to El Niño-induced drought," in Proceedings of the National Academy of Sciences, 9204–9209. doi:10.1073/pnas.1524888113*Proc. Natl. Acad. Sci. U. S. A.* 113.
- Filonchyk, M. (2022). Characteristics of the severe March 2021 Gobi Desert dust storm and its impact on air pollution in China. *Chemosphere* 287, 132219. doi:10.1016/j. chemosphere.2021.132219
- Giglio, L. (2007). Characterization of the tropical diurnal fire cycle using VIRS and MODIS observations. *Remote Sens. Environ.* 108, 407–421. doi:10.1016/j.rse.2006. 11.018
- Herman, J. R., and Celarier, E. (1997). Earth surface reflectivity climatology at 340–380 nm from TOMS data. *J. Geophys. Res.* 102, 28003–28011. doi:10.1029/97JD02074
- Jain, P., Barber, Q. E., Taylor, S. W., Whitman, E., Castellanos Acuna, D., Boulanger, Y., et al. (2024). Drivers and impacts of the record-breaking 2023 wildfire season in Canada. *Nat. Commun.* 15, 6764. doi:10.1038/s41467-024-51154-7
- Jethva, H., Torres, O., Remer, L. A., and Bhartia, P. K. (2013). A color ratio method for simultaneous retrieval of aerosol and cloud optical thickness of above-cloud absorbing aerosols from passive sensors: application to MODIS measurements. *IEEE T. Geosci. Remote Sens.* 51, 3862–3870. doi:10.1109/TGRS.2012.2230008
- Jing, L., Wong, M., Shi, G., Nichol, J., Lee, K., and Chan, P. W. (2024). Advanced algorithms on monitoring diurnal variations in dust aerosol properties using geostationary satellite imagery. *Remote Sens. Environ.* 303, 0034–4257. doi:10.1016/j. rse.2024.113996
- Kayetha, V., Torres, O., and Jethva, H. (2022). Retrieval of UV-visible aerosol absorption using AERONET and OMI-MODIS synergy: spatial and temporal variability across major aerosol environments. *Atmos. Meas. Tech.* 15, 845–877. doi:10.5194/amt-15-845-2022
- Kim, M., Kim, J., Torres, O., Ahn, C., Kim, W., Jeong, U., et al. (2018). Optimal estimation-based algorithm to retrieve aerosol optical properties for GEMS measurements over Asia. *Remote Sens.* 10, 162. doi:10.3390/rs10020162
- Kim, J., Jeong, U., Ahn, M. H., Kim, J. H., Park, R. J., Lee, H., et al. (2020). New era of air quality monitoring from space: geostationary environment monitoring spectrometer (GEMS). *B. Am. Meteor. Soc.* 101, E1–E22. doi:10.1175/BAMS-D-18-0013.1
- Li, F., Zhang, X., Roy, D. P., and Kondragunta, S. (2019). Estimation of biomass-burning emissions by fusing the fire radiative power retrievals from polar-orbiting and geostationary satellites across the conterminous United States. *Atmos. Environ.* 211, 274–287. doi:10.1016/j.atmosenv.2019.05.017
- Luo, J., Huang, F., Gao, S., Liu, S., Liu, R., and Devasthale, A. (2022). Satellite monitoring of the dust storm over Northern China on 15 march 2021. *Atmosphere* 13, 157. doi:10.3390/atmos13020157
- Malingreau, J. P., Stephens, G., and Fellows, L. (1985). Remote-sensing of forest fires kalimantan and North Borneo in 1982-83. *Ambio* 14 (6), 314–321. Available online at: http://www.jstor.org/stable/4313177.
- Marshak, A., Herman, J., Szabo, A., Blank, K., Cede, A., Carn, S., et al. (2018). Earth observations from DSCOVR EPIC instrument. *Bull. Am. Meteorol. Soc.* 99, 1829–1850. doi:10.1175/BAMS-D-17-0223.1
- Marsham, J. H., and Ryder, C. L. (2021). Dust storms and haboobs. Weather 76, 378–379. doi:10.1002/wea.4071
- Meyer, K., Platnick, S., and Zhang, Z. (2015). Simultaneously inferring above-cloud absorbing aerosol optical thickness and underlying liquid phase cloud optical and microphysical properties using MODIS. *J. Geophys. Res.-Atmos.* 120, 5524–5547. doi:10.1002/2015JD023128
- Mu, M., Randerson, J. T., van der Werf, G. R., Giglio, L., Kasibhatla, P., Morton, D., et al. (2011). Daily and 3-hourly variability in global fire emissions and consequences for atmospheric model predictions of carbon monoxide. *J. Geophys. Res.* 116, D24303. doi:10.1029/2011JD016245
- NASA/LARC/SD/ASDC (2019). DSCOVR EPIC level 2 UV Aerosol version 3. NASA Langley Atmos. Sci. Data Cent. DAAC. doi:10.5067/EPIC/DSCOVR/L2_AER_03
- Ohneiser, K., Ansmann, A., Witthuhn, J., Deneke, H., Chudnovsky, A., Walter, G., et al. (2023). Self-lofting of wildfire smoke in the troposphere and stratosphere:

simulations and space lidar observations. Atmos. Chem. Phys. 23, 2901–2925. doi:10. 5194/acp-23-2901-2023

- Page, S. E., Siegert, F., Rieley, J. O., Boehm, H. D. V., Jaya, A., and Limin, S. (2002). The amount of carbon released from peat and forest fires in Indonesia during 1997. *Nature* 420, 61–65. doi:10.1038/nature01131
- Peterson, D. A., Campbell, J. R., Hyer, E. J., Fromm, M. D., Kablick, G. P., Cossuth, J. H., et al. (2018). Wildfire driven thunderstorms cause a volcano-like stratospheric injection of smoke. *Clim. Atmos. Sci.* 1, 30. doi:10.1038/s41612-018-0039-3
- Pliscoff, P., Folchi, M., Aliste, E., Cea, D., and Simonetti, J. A. (2020). Chile mega-fire 2017: an analysis of social representation of forest plantation territory. *Appl. 871 Geogr.* 119, 102226. doi:10.1016/j.apgeog.2020.102226
- Rein, G., Cleaver, N., Ashton, C., Pironi, P., and Torero, J. L. (2008). The severity of smouldering peat fires and damage to the forest soil. *Catena* 74 (3), 304–309. doi:10. 1016/j.catena.2008.05.008
- Rogers, C. M., and Bowman, K. P. (2001). Transport of smoke from the Central American fires of 1998. *J. Geophys. Res.-Atmos.* 106, 28357–28368. doi:10.1029/2000JD000187
- Romme, W. H., and Despain, D. G. (1989). Historical perspective on the Yellowstone fires of 1988. Bioscience 39 (10), 695-699. doi:10.2307/1311000
- Seiler, W., and Crutzen, P. J. (1980). Estimates of gross and net fluxes of carbon between the biosphere and the atmosphere from biomass burning. *Clim. Change* 2, 207–247. doi:10.1007/BF00137988
- Seinfeld, J. H., Bretherton, C., Carslaw, K. S., Coe, H., DeMott, P. J., Dunlea, E. J., et al. (2016). Improving our fundamental understanding of the role of aerosol-cloud interactions in the climate system. *Proc. Natl. Acad. Sci. U. S. A.* 113, 5781–5790. doi:10.1073/pnas.1514043113
- Tang, W., Emmons, L. K., Buchholz, R. R., Wiedinmyer, C., Schwantes, R. H., He, C., et al. (2022). Effects of fire diurnal variation and plume rise on U.S. air quality during FIREX-AQ and WE-CAN based on the multi-scale infrastructure for chemistry and aerosols (MUSICAv0). *J. Geophys. Res. Atmos.* 127 (16), e2022JD036650. doi:10.1029/2022JD036650
- Torres, O., and Ahn, C. (2024). Local and regional diurnal variability of aerosol properties retrieved by DSCOVR/EPIC UV algorithm. *J. Geophys. Res. Atmos.* 129, e2023JD039908. doi:10.1029/2023JD039908
- Torres, O., and Remer, L. (2013). "History of passive remote sensing of aerosol from space," in *ch.7 in aerosol remote sensing*. Editors J. Lenoble, L. Remer, and D. Tanre (Springer-Praxis). 978-3-642-17724-8. doi:10.1007/978-3-642-17725-5
- Torres, O., Jethva, H., and Bhartia, P. K. (2012). Retrieval of aerosol optical depth above clouds from OMI observations: sensitivity analysis and case studies. *J. Atmos. Sci.* 69, 1037–1053. doi:10.1175/JAS-D-11-0130.1
- Torres, O., Bhartia, P. K., Taha, G., Jethva, H., Das, S., Colarco, P., et al. (2020). Stratospheric injection of massive smoke plume from Canadian boreal fires in 2017 as seen by DSCOVR-EPIC, CALIOP, and OMPS-LP observations. *J. Geophys. Res. Atmos.* 125 (10), e2020JD032579. doi:10.1029/2020JD032579
- von Hoyningen-Huene, W., Schmidt, T., Schienbein, S., Kee, C. A., and Tick, L. J. (2012). Climate-relevant aerosol parameters of South-East Asian forest re haze. *Atmos. Environ.* 33, 3183–3190. doi:10.1016/S1352-2310(98)00422-1
- Wang, Z., Wang, Z., Zou, Z., Chen, X., Wu, H., Wang, W., et al. (2024). Severe global environmental issues caused by Canada's record-breaking wildfires in 2023. *Adv. Atmos. Sci.* 41 (4), 565–571. doi:10.1007/s00376-023-3241-0
- Xu, X., Wang, J., Wang, Y., Zeng, J., Torres, O., Yang, Y., et al. (2017). Passive remote sensing of altitude and optical depth of dust plumes using the oxygen A and B bands: first results from EPIC/DSCOVR at Lagrange-1 point. *Geophys. Res. Lett.* 44, 7544–7554. doi:10.1002/2017GL073939
- Xu, X., Wang, J., Wang, Y., Zeng, J., Torres, O., Reid, J. S., et al. (2019). Detecting layer height of smoke aerosols over vegetated land and water surfaces *via* oxygen absorption bands: hourly results from EPIC/DSCOVR in deep space. *Atmos. Meas. Tech.* 12, 3269–3288. doi:10.5194/amt-12-3269-2019
- Yasunari, T. J., Narita, D., Takemura, T., Wakabayashi, S., and Takeshima, A. (2024). Comprehensive impact of changing Siberian wildfire severities on air quality, climate, and economy: MIROC5 global climate model's sensitivity assessments. *Earth's Future* 12, e2023EF004129. doi:10.1029/2023EF004129
- Yu, H., Tan, Q., Zhou, L., Zhou, Y., Bian, H., Chin, M., et al. (2021). Observation and modeling of the historic "Godzilla" African dust intrusion into the Caribbean Basin and the southern US in June 2020. *Atmos. Chem. Phys.* 21, 12359–12383. doi:10.5194/acp-21-12359-2021
- Zhang, X., Kondragunta, S., Ram, J., Schmidt, C., and Huang, H.-C. (2012). Near-real-time global biomass burning emissions product from geostationary satellite constellation. *J. Geophys. Res.* 117, D14201. doi:10.1029/2012JD017459
- Zhang, S., Solomon, S., Boone, C. D., and Taha, G. (2024). Investigating the vertical extent of the 2023 summer Canadian wildfire impacts with satellite observations. *Atmos. Chem. Phys.* 24, 11727-11736. doi:10.5194/acp-24-11727-2024
- Zoogman, P., Liu, X., Suleiman, R., Pennington, W., Flittner, D., Al-Saadi, J., et al. (2017). Tropospheric emissions: monitoring of pollution (TEMPO). *J. Quant. Spectrosc. Radiat. Transf.* 186, 17–39. doi:10.1016/j.jqsrt.2016.05.008